Anomalies in the response of V, Nb, and Ta to tensile and shear loading: *Ab initio* density functional theory calculations

Naoyuki Nagasako,[1,*] Michal Jahnátek,[2,†] Ryoji Asahi,[1,‡] and Jürgen Hafner[2,§]
[1]*Toyota Central Research and Development Laboratories Inc., Nagakute, Aichi 480-1192, Japan*
[2]*Faculty of Physics and Center for Computational Materials Science, University of Vienna, Sensengasse 8/12, A-1090 Wien, Austria*
(Received 21 December 2009; revised manuscript received 9 February 2010; published 17 March 2010)

Ab initio density functional calculations of the response of V, Nb, and Ta to tensile and shear loading have been performed. We find that the behavior of all three metals of the V group under large strains differs considerably from that reported for the other body-centered cubic (bcc) transition metals (Mo, W, and Fe). Under unaxial ⟨100⟩ tensile loading, V and Nb undergo a bifurcation from a tetragonal to an orthorhombic deformation path, associated with a shear instability, before reaching the stress maximum. The bifurcation strongly reduces the ideal tensile strengths to 11.5 GPa for V and 12.5 GPa for Nb. For Ta the bifurcation point coincides with the stress maximum of 13.6 GPa along the tetragonal path so that the metal fails under tensile strain by shear and not by cleavage. The stress-strain curves calculated for the {110}⟨111⟩ and {211}⟨111⟩ slip systems are strongly asymmetric; the ideal shear strengths for both slip systems are 6.5 (5.5) GPa for V and 7.8 (6.0) GPa for Nb. Hence the ideal shear strengths are only half as large as for the bcc metals Mo and W, but much larger than expected on the basis for the low shear moduli of V and Nb. Ta shows a behavior intermediate between these two groups of metals, with a calculated ideal shear strength of 7.1 (6.5) GPa, in excellent agreement with the experimental estimate from nanoindentation experiments. The saddle-point structure determining the shear strength for both slip systems is a special body-centered-tetragonal structure. This structure is identical to the saddle-point structure identified on the orthorhombic deformation path under uniaxial tension. Hence also V and Nb will fail under uniaxial tension not by cleavage, but by shear.

DOI: 10.1103/PhysRevB.81.094108 PACS number(s): 61.72.Nn, 62.25.−g, 62.20.F−

I. INTRODUCTION

The strength of any solid is limited by the ideal or theoretical strength defined by the stress required to yield or break a perfect crystal. The ideal shear strength determines the stress necessary for the nucleation of dislocations, while for the formation of a cleavage crack the local stress must exceed the ideal tensile strength.[1] In real solids the maximum attainable stress is strongly influenced by the formation of mobile dislocations, by grain boundaries, cracks, and other microstructural features, but it can never exceed the ideal value. While no experimental determinations of the ideal strength under tension have been possible to date, the ideal shear strength can be estimated from nanoindentation experiments.[2–6] In nanoindentation experiments the indenter is so small that the volume of the probe undergoing shear deformation may be considered as defect free. In a typical nanoindentation test force and displacement are recorded as the indenter tip is pressed into the materials surface. The yield stress is identified by the first point at which the experimental data deviate from the elastic curve. At this point the indenter moves into the substrate without a measurable increase of the load—this is usually interpreted as a homogeneous dislocation nucleation event.[5,6] However, a detailed analysis of the load/displacement curves and detailed molecular dynamics simulations suggest that the nominally "elastic" part of the curve might contain some superimposed plastic deformation too subtle to be detected. This would mean that even nanoindentation experiments can seriously underestimate the theoretical strength. For example, Biener *et al.*[4] derived for body-centered cubic Ta a maximal shear stress of 7.5 GPa, considerably below the theoretical shear strength of 11 GPa estimated from the shear modulus of 69 GPa.

In view of the difficulty to determine the ideal strength in experiments, there is a continuing interest in its theoretical calculations. The earliest attempts assumed a simple analytic form of the stress-strain curve which allows to derive the ideal strength from the elastic moduli.[1,7] This allows to define a dimensionless shear and tensile strength, $\sigma^\star = \sigma_{max}/E$ and $\tau^\star = \tau_{max}/G$, where σ_{max} and τ_{max} are the maxima of tensile and shear stress and E and G are the experimental values of the Young's modulus and the shear modulus for the direction of loading. The reduced dimensionless shear and tensile strengths are assumed to be essentially constant for a specific class of materials. A significant step forward was realized since the 1970s using atomistic models based on empirical or semiempirical force fields which provided valuable information on the atomistic mechanisms of the deformation under large strains.[8–12] However, because the parameters of the force fields were necessarily fitted to the materials properties at small strains, the predictions cannot be considered as quantitatively reliable. Finally since the 1990s *ab initio* density functional calculations began to supercede empirical methods for the determination of the response of metals and intermetallic compounds to tensile and shear loading.[13–24] These methods are free from adjustable parameters, valid at all strains and permit in principle a quantitative determination of the ideal strengths. However, because of the relatively large computational effort required in such calculations, early studies were performed at fixed strains.[13,14] In this case the selected strain was stepwise increased by small increments while the other five independent strains were fixed at zero, i.e., all internal relaxations were suppressed.

More meaningful results for the energy-strain and stress-strain relations are achieved if the crystal is relaxed until only the stress conjugate to the applied strain has a nonzero value. A review of semiempirical and *ab initio* calculations of ideal tensile and shear strengths has recently been compiled by Pokluda *et al.*[25]

Even to date, *ab initio* calculations of tensile and shear strengths are available only for a few selected metals and for a very few intermetallic compounds. The face-centered cubic (fcc) metals Al (Refs. 18, 22–24, and 26–29) and Cu (Refs. 18, 22–24, 30, and 31) have been studied most extensively. Among the body-centered cubic metals attention was focused on Fe (Refs. 32 and 33) and on the refractory metals Mo and W.[16,19,21]

The studies of the fcc metals Al and Cu have emphasized that estimates of the ideal strength based on the elastic behavior are of limited validity: for both $\{111\}\langle 11\bar{2}\rangle$ and $\{111\}\langle \bar{1}10\rangle$ shear deformations, the shear constants of Cu are much higher than those of Al, while from the position of the maximum on the stress-strain curve a higher ideal shear strength is predicted for Al.[24,28] The investigations of the loading behavior of the fcc metals have also demonstrated that the theoretical strength may be limited by a shear-related instability, by the softening of a phonon mode along a tensile deformation path or by stacking-fault formation along a shear deformation path, even before the maximum in the stress-strain curve has been reached. For example, the ideal tensile strength (ITS) of Cu under [100] loading is limited by the occurrence of a shear instability[30,34] at a strain of 10%. The instability induces a bifurcation from a tetragonal to an orthorhombic deformation path and limits the ITS to 9.5 GPa, compared a stress maximum of 23.8 GPa at a strain of 36.0%. For Al Clatterbuck *et al.*[26] have reported phonon instabilities under uniaxial [100] tension at strains of 17% and 18% limiting the ITS to 9.2 GPa compared to a peak value of 12.9 GPa, under [110] tension a soft phonon mode appears at a strain of 11%. In all cases the soft phonon modes show displacement patterns corresponding to periodic shear deformations. For Al under both $\{111\}\langle 11\bar{2}\rangle$ and $\{111\}\langle \bar{1}10\rangle$ shear deformations the ideal shear strength (ISS) is limited by (i) stacking fault instabilities and (ii) soft phonon modes.[24,26] Under $\{111\}\langle 11\bar{2}\rangle$ shear the unstable stacking fault configuration is reached at a strain of 14.5%, at the same strain a phonon instability has been reported. The displacement of the soft phonon mode corresponds to $\{111\}\langle 11\bar{2}\rangle$ shear failure with a periodicity of two or three {111} planes, it is also closely related to the failure mode induced by the soft phonon mode predicted for [110] tension (for a detailed discussion we refer to Jahnátek *et al.*)[24] For fcc Cu, no shear instabilities occur under uniaxial [110] or [100] tensile loading. Also, in contrast to Al the unstable stacking fault configurations under $\{111\}\langle 11\bar{2}\rangle$ and $\{111\}\langle \bar{1}10\rangle$ shear deformations are reached only at strains beyond the maximum on the stress-strain curve.[23,24,34]

In comparison to this very complex scenario, the investigations of the bcc metals presented so far describe a much simpler picture. Investigations of tensile loading have concentrated on the $\langle 100\rangle$ directions because symmetry considerations,[12] early *ab initio* calculations[16] and empirical tests have all identified the $\langle 100\rangle$ directions as the weak directions in tension and the {100} planes as cleavage planes. The general theory of the response of cubic metals to uniaxial loading along $\langle 100\rangle$ has been developed in a series of classical papers by Milstein *et al.*[10,11] Starting from an unstressed bcc structure all metals first adopt a primary deformation path with tetragonal guiding symmetry. Any deviation from tetragonality implies the presence of a transverse load. However, as already shown by Hill and Milstein[8] at a "special invariant state" where the elastic constants satisfy the condition $c_{22}=c_{23}$, a bifurcation to a secondary orthorhombic path may occur under dead load (note that the invariance condition implies a tetragonal shear instability). For the refractory bcc metals Mo and W (Refs. 19 and 21) and for bcc Fe (Ref. 32) it has been shown that the tetragonal symmetry is broken only after the point of maximum tensile stress has been passed. Only for bcc Nb the bifurcation occurs already at a lower strain and leads to an ITS which is significantly lower (13.1 GPa) than that on the tetragonal path (18.8 GPa). Shear deformations along $\langle 111\rangle$ may occur in bcc crystals by slip on the (110), (112), and (123) planes. All three shear systems have been studied by Roundy *et al.*[19] for W, while for Mo, Nb, and Fe only the two first have been investigated. The stress-strain curves are very similar for [111] slip along all investigated glide planes, leading to similar values of the ISS. A remarkable result is that for all bcc metals with the exception of Nb the reduced dimensionless tensile and shear strengths are very close to the ideal values, $\sigma^{\star}=\sigma_{max}/E=0.08$ and $\tau^{\star}=\tau_{max}/G=0.11$, calculated under the assumption of a sinusoidal stress-strain curve with a period that is twice the strain required to reach the saddle-point structure determining the ideal strength (i.e., the fcc phase in tension and a body-centered tetragonal phase under shear). The stress-strain curve of Nb under shear shows a strong deviation with a low initial slope caused by a low shear modulus, the reduced ideal shear strength is $\tau^{\star}=0.18$, i.e., 50% higher than for the other bcc metals. Together these results show that among all investigated bcc metals Nb is the only one that is predicted to fail by $\{211\}\langle 111\rangle$ shear rather than by [100] tensile failure. In very recent work[35] the effect of a superposed transverse stress has been considered. As observed for other metals, hydrostatic tension raises, while hydrostatic compression lowers the ITS of Nb.

The exceptional behavior of Nb under tensile and shear loading has been attributed to a very low $G_{\langle 111\rangle}/E_{\langle 100\rangle}$ ratio were the relaxed modulus for [100] tension is given by

$$E_{\langle 100\rangle}=\frac{(c_{11}-c_{12})(c_{11}+2c_{12})}{c_{11}+c_{12}}, \tag{1}$$

and

$$G_{\langle 111\rangle}=\frac{3c_{44}(c_{11}-c_{12})}{4c_{44}+c_{11}-c_{12}}, \tag{2}$$

is the relaxed modulus for shear along $\langle 111\rangle$ (note that because of the threefold rotational symmetry around the $\langle 111\rangle$ axes, any shear in this direction has the same modulus). Using the experimental values of the elastic constants[36–40] this

ratio is G/E=0.34, 0.28, and 0.42 for V, Nb, and Ta, and G/E=0.35 and 0.39 for Mo and W. This would suggest that the anomalous behavior under tensile and shear loading should be restricted to Nb, while V and Ta should be expected to behave similarly as Mo and W. However, it is well known that Nb and V share some interesting anomalies in their elastic, dynamic, and superconducting properties: (i) low values of the trigonal and tetragonal shear constants (c_{44}=43, 29, and 83 GPa for V, Nb, and Ta; $c'=(c_{11}-c_{12})/2$=55.5, 57 and 53 GPa for V, Nb, and Ta). (ii) Theoretical calculations[41,42] predict a pronounced softening of the trigonal shear modulus of V and Nb under compression, driving a mechanical instability of bcc V while for Nb the shear modulus softens for pressures around 50 GPa, but remains positive. The occurrence of a structural phase transition of V from bcc to a rhombohedral phase at about 63–69 GPa has recently been confirmed by synchrotron x-ray diffraction.[44] In contrast the absence of pressure-induced phase transitions in Nb up to 145 GPa has recently been confirmed.[45] (iii) The elastic anomalies of V and Nb are reflected in anomalies of their phonon dispersion relations.[46–48] (iv) Phonon softening is thought to be responsible for the high superconducting transition temperature T_c in Nb and for the strong increase of T_c under compression in V.

The elastic and phonon anomalies have been discussed extensively in relation to the electronic properties and shown to be related to the nesting properties of the Fermi surface.[42,49] In particular, the downward dispersion of the transverse phonon branch along [100] and therefore also the unusual softness of c_{44} has been shown to arise from the nesting properties of the Fermi surface around the N point leading to a van Hove singularity in the electronic density of states close to the Fermi energy.

Here we present an extended study of the response of all three V-group metals to tensile and shear loading based on *ab initio* density functional calculations. Our calculations allow for a bifurcation from a tetragonal to an orthorhombic deformation path under uniaxial tensile strain. Shear deformations have been studied for the $\{110\}\langle 111\rangle$ and $\{211\}\langle 111\rangle$ shear systems.

II. COMPUTATIONAL METHODS

Our *ab initio* total-energy and force calculations are based on density functional theory (DFT) as implemented in the Vienna *ab initio* simulation package (VASP).[50,51] A gradient-corrected functional has been used to describe electronic exchange and correlations.[52] Electron-ion interactions are treated within the projector-augmented wave (PAW) method.[53,54] For all elements we used the standard PAW pseudopotentials (PP) distributed with VASP with reference configurations $np^6nd^4(n+1)s^1$ for the valence states with n=3,4, and 5 for V, Nb, and Ta. The plane-wave basis set contained components with kinetic energies up to 350 eV.

The response of the crystal to tensile or shear deformations was calculated by increasing the strain along the chosen directions in small steps. Increasing/decreasing the strain by very small increments leads to a reversible deformation process at zero absolute temperature with negligible hysteresis. The crystal structure was fully relaxed at each deformation step until all lateral stresses vanished. This has been done by the efficient external optimizer GADGET developed by Bučko *et al.*[55] GADGET performs a relaxation in terms of generalized coordinates which allow a better control of lateral stresses. The forces acting on the atoms were computed via the Hellmann-Feynman theorem,[56] the stress tensor acting on the unit cell was computed via the generalized virial theorem.[57] The use of a high cut-off energy allows to achieve a high accuracy of the components of the stress tensor. The Brillouin zone (BZ) was sampled using various types of meshes according to the size and symmetry of the computational cells. Because the elastic properties and the stresses at small strains of V and Nb are strongly influenced by the occurrence of van Hove anomalies close to the Fermi level, very fine k-point meshes (up to $23\times23\times23$ for calculations based on a simple face-centered or body-centered tetragonal cell and up to $22\times14\times8$ for the larger supercells used for simulating shear deformations) are required to calculate the elastic shear constants and the stress-strain relations. All integration meshes were constructed according to the Monkhorst-Pack scheme.[58] The integration over the BZ used the Methfessel-Paxton method[59] with the smearing parameter of 0.2 eV for calculation of the total energies and stresses, and the tetrahedron method with Blöchl corrections[60] for the calculation of the density of states. The total energy was calculated with high precision, converged to 10^{-8} eV/atom. The structural relaxation was stopped when all forces acting on the atoms where converged to within 10^{-3} eV/Å and all components of the stress tensor except that conjugate to the imposed strain where converged to within 0.05 GPa.

For the calculation of the elastic constants we used the linear-interpolation method of the stress tensors. The cubic cells were submitted to the $\pm\varepsilon_1$ and $\pm\varepsilon_4$ strains; the tetragonal cells were submitted in addition to $\pm\varepsilon_3$ and $\pm\varepsilon_6$ strains; for the orthorhombic cells two more strains, $\pm\varepsilon_2$ and ε_5; were added. For each set of strains $\pm\varepsilon_i$ two different magnitudes of 0.2% and 0.5% were used. For the calculation of the elastic constants the total energy was calculated with even higher accuracy, converged to 10^{-9} eV/atom.

III. ELASTIC PROPERTIES

The elastic constants of the V-group metals, together with the Young's modulus $E_{\langle 100\rangle}$ for tension along $\langle 100\rangle$ and the relaxed shear modulus $G_{\langle 111\rangle}$ for shear along the $\langle 111\rangle$ direction are compiled in Table I. It is well known that although very good agreement for the bulk modulus $[B=(c_{11}+2c_{12})/3]$ and the orthorhombic shear constant $c'=(c_{11}-c_{12})/2$ is achieved, all DFT calculations seriously underestimate the trigonal shear constant c_{44}, irrespective of the exchange-correlation functional (local or semilocal gradient-corrected functional) and of the method used for solving the Kohn-Sham equations (plane-wave based pseudopotential or PAW calculations, muffin-tin orbital methods).[41–43] The low value of the trigonal shear constant is related to an anomalous dispersion of transverse acoustic phonons propagating along the $\langle 100\rangle$ direction. In the long-wavelength limit, shear constant, and frequencies of transverse acoustic phonons are

TABLE I. Elastic constants, shear anisotropy $A=2(c'-c_{44})/c_{44}$, relaxed tensile modulus $E_{\langle 100\rangle}$, relaxed shear modulus $G_{\langle 111\rangle}$, and ratio G/E for the body-centered cubic metals of the V group (in GPa).

Metal	Reference	c_{11}	c_{12}	c_{44}	$c'=(c_{11}-c_{12})/2$	A	$E_{\langle 100\rangle}$	$G_{\langle 111\rangle}$	G/E
V	This work	262	144	17	59	4.9	160	32	0.20
	Theory, Ref. 42	260	135	17	63	5.4	168	33	0.20
	Theory, Ref. 43	205	130	5	37.5	13.0	104	12	0.11
	Exp., Ref. 37	231	120	43	55.5	0.56	149	50	0.33
Nb	This work	247	138	17	54.5	4.4	148	31	0.21
	Theory, Ref. 42	247	138	10	54.5	8.9	148	22	0.15
	Theory, Ref. 43	267	147	27	60	2.4	163	43	0.26
	Exp., Ref. 37	246	133	29	57	1.9	154	43	0.28
Ta	This work	257	163	71	47	−0.68	132	53	0.40
	Theory, Ref. 42	265	159	74	53	−0.57	146	59	0.40
	Theory, Ref. 43	291	162	84	64.5	−0.46	175	70	0.40
	Exp., Ref. 37	266	161	83	53	−0.72	145	60	0.41
Mo	This work	470	161	105	154	0.93	386	133	0.34
	Theory, Ref. 43	406	150	107	128	0.40	325	120	0.37
	Exp., Ref. 37	465	162	109	152	0.78	381	134	0.35
W	This work	500	205	130	148	0.27	382	142	0.37
	Theory, Ref. 43	553	207	178	173	−0.06	440	175	0.40
	Exp., Ref. 37	523	204	161	159	0.03	407	159	0.39

related through $c_{44}=\omega^2(q)\rho/q^2$ where ρ is the density. Softening of acoustic phonons and the low value of the shear constant are related to the nesting properties of the Fermi surface which produce a van Hove singularity in the electronic density of states (DOS) close to the Fermi level, as discussed in detail by Landa *et al.*[41] As shown in Fig. 1, the distance between the van-Hove peak in the DOS and the Fermi energy increases from V to Nb and Ta, in correspondence to an increasing value of the shear constant. Due to the presence of the van-Hove singularity, an exact determination of c_{44} requires a very fine mesh for Brillouin zone integrations. With a $23\times23\times23$ grid, full convergence is achieved, but the shear constant is still too low by a factor of about two. It is well known that crystalline imperfections tend to smear out the Fermi surface and hence the singularity in the DOS and that this results in a damping of the related anomalies in the phonon dispersion relations and to a stiffening of the elastic shear modes. In theoretical calculations this effect may be modeled by applying a Gaussian smearing to the eigenstates and we find that a broadening of the energy levels leads to a larger value of the c_{44} shear constant. While this might account for part of the discrepancy between theory and experiment, more accurate experiments at low temperatures and high-quality specimens would also be desirable. For the moment we note that the very low values resulting from all theoretical calculations should be treated with caution, although the trends among the V-group metals are at least semiquantitatively correct. We also note that for the relaxed tensile and shear moduli relevant to the present study, agreement between theory and experiment is better than for c_{44} alone. To assess the validity of our method for calculating the elastic constants of bcc transition metals we include in Table I our results for Mo and W, together with the experimental values. For both metals we note very good agreement between theory and experiment.

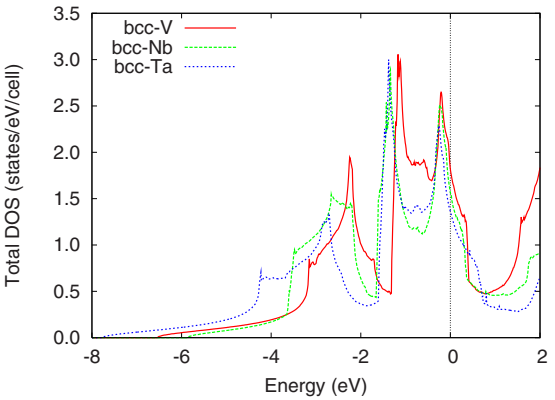

FIG. 1. (Color online) Electronic density of states of bcc V, Nb, and Ta. Note the van-Hove singularities close to the Fermi level.

IV. RESPONSE TO UNIAXIAL [100] TENSILE LOADING

The general theory of the response of cubic metals to uniaxial ⟨100⟩ loading has been formulated by Milstein *et al.*[8,9,11] On the primary tetragonal deformation path (the Bain path) the structure can be considered as either body-centered tetragonal (bct) or face-centered tetragonal (fct). By symmetry only three stress-free states are possible: bcc, fcc, and a special bct (or equivalently fct) structure, but the order of appearance of these states along the deformation path depends on the details of interatomic binding. Owing to crystal symmetry, the fcc state can be reached from the bcc state

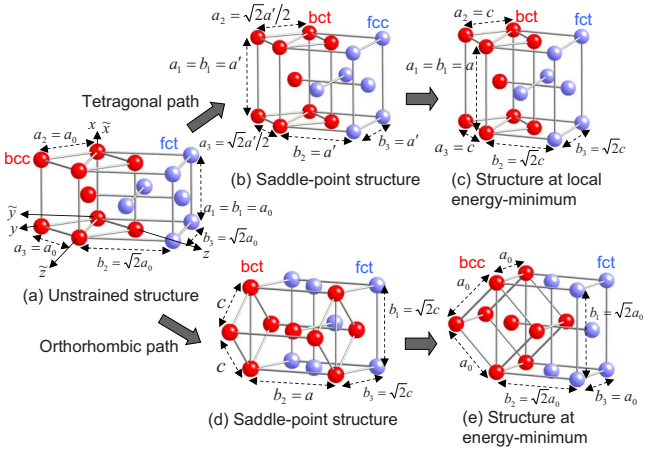

FIG. 2. (Color online) Sketch of the PTP and SOP deformation paths of a body-centered cubic lattice shown in red (black) under uniaxial [100] tensile loading. The structures along the PTP are described within the body-centered tetragonal reference frame (lattice constants $a_i, i=1-3$), those along the SOP are described as face-centered tetragonal [shown in blue (gray)—lattice constants $b_i, i=1-3$].

only by applying uniaxial tension, hence there are three possible orderings of the stress-free states: (1) bcc, bct, fcc (as found for the alkali metals),[11] (2) bct, bcc, fcc, and (3) bcc, fcc, bct. The centrally located stress-free state is necessarily unstable because of a decreasing stress at increasing strain, it represents a saddle point on the energy-strain curve. Scenario (3) is realized along the tetragonal deformation path of the bcc transition metals such as W.[18–20] If the primary tetragonal path (PTP) contains the "special invariant state" where $c_{22}=c_{23}$, a bifurcation to a secondary orthorhombic path (SOP) can occur under strict uniaxial load. Immediately after bifurcation the system passes through a stress-free bct state while at larger strain the original bcc structure is recovered.

Figure 2(a) shows a sketch of the bcc lattice embedded into a more general fct lattice. Tetragonal deformations can be described by the variation of the lattice parameters a_1 and $a_2=a_3$ of a bct lattice with a_1 increasing linearly as a function of strain. The deformations along an orthorhombic deformation path can be described in terms of a fct lattice with $b_1=a_1=a_0$ and $b_2=b_3=\sqrt{2}a_0$ in the undeformed state. Along the PTP relaxation minimizes the total energy with respect to $a_2=a_3$ only, while along the SOP the total energy is minimized independently with respect to both b_2 and b_3.

The energy-strain and stress-strain curves, as well as the variation in the lattice parameters a_i and b_i as a function of strain are shown for V, Nb, and Ta in Figs. 3–5. As a measure of strain we use the engineering strain. The scenario is qualitatively the same for all three metals, albeit with some important quantitative differences. Along the PTP the maximum on the energy-strain curve is the fcc structure as shown in Fig. 2(b). Under a volume-conserving deformation the strain at which the bct cell assumes the fcc structure is given by the Bain strain of $\epsilon_B=\sqrt[3]{2}-1=0.26$. For all three metals the fcc structure is realized at a slightly larger strain varying from $\epsilon=0.274$ for V to $\epsilon=0.273$ for Nb and $\epsilon=0.271$ for Ta,

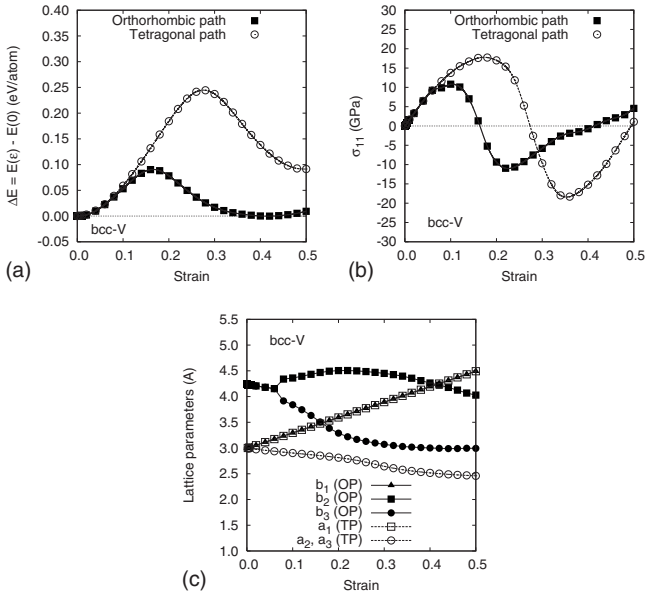

FIG. 3. Variation in (a) the total energy, (b) the stress, and (c) the lattice constants of bcc V under [100] tension as a function of the applied strain. Open symbols refer to the primary tetragonal deformation path, closed symbols to the secondary orthorhombic deformation path. The bifurcation from the PTP to the SOP occurs at a strain of 0.06.

corresponding to a slight volume expansion. Upon further increased tensile strain the total energy reaches a minimum for a special bct structure at $\epsilon=0.494$ for V, $\epsilon=0.479$ for Nb and at $\epsilon=0.438$ for Ta. The ITS and the critical strains for all three metals calculated along the PTP are compiled in Table

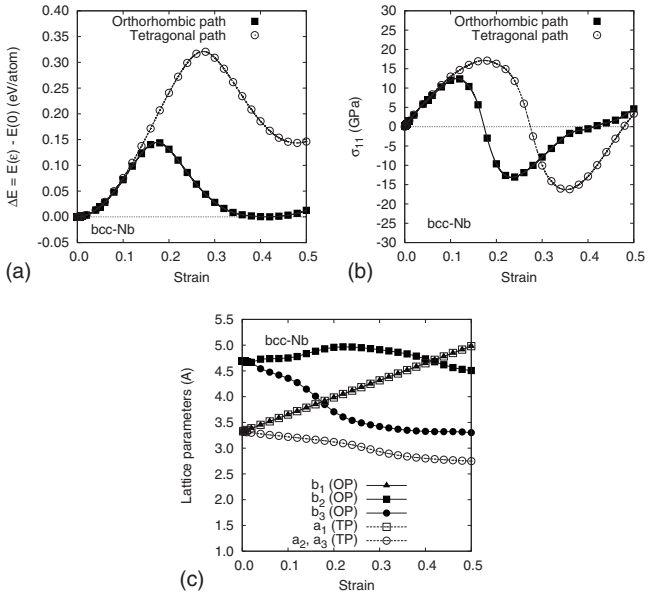

FIG. 4. Variation in (a) the total energy, (b) the stress, and (c) the lattice constants of bcc Nb under [100] tension as a function of the applied strain. Open symbols refer to the primary tetragonal deformation path, closed symbols to the secondary orthorhombic deformation path. The bifurcation from the PTP to the SOP occurs at a strain of 0.05.

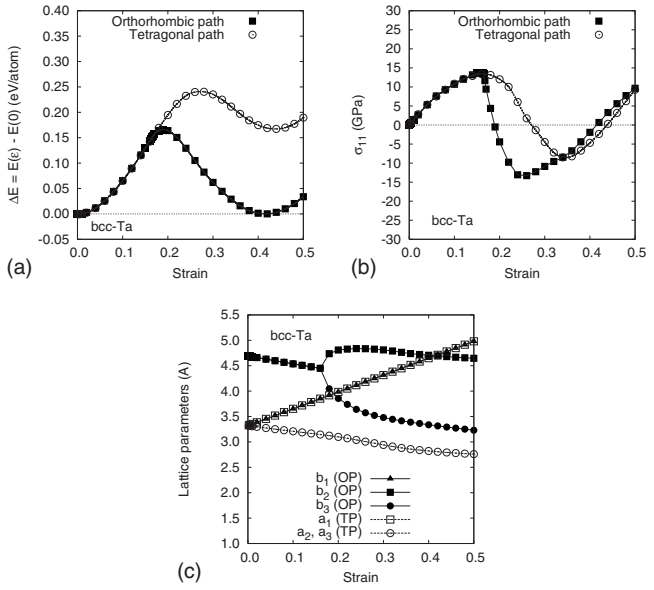

FIG. 5. Variation in (a) the total energy, (b) the stress, and (c) the lattice constants of bcc Ta under [100] tension as a function of the applied strain. Open symbols refer to the primary tetragonal deformation path, closed symbols to the secondary orthorhombic deformation path. The bifurcation from the PTP to the SOP (equivalent to a shear instability of the bct lattice) occurs at a strain of $\epsilon = 0.16$, i.e., it is almost coincident with the stress maximum along the PTP.

II. For Nb we note a very good agreement with the results of Luo *et al.*[21] The dimensionless ITSs $\sigma^{\star}=\sigma_{max}/E_{\langle 100\rangle} \sim 0.10-0.11$ reached along the PTP are somewhat larger than those calculated of bcc Mo and W, reflecting a modest asymmetry of the stress-strain curve.

If the constraint of a tetragonal guiding symmetry is relaxed, a bifurcation to the SOP occurs at low values of the critical strain, $\epsilon_c=0.06$ and 0.05 for V and Nb, but only at $\epsilon_c=0.16$ for Ta. For Ta this critical strain is almost identical to the critical strain at which the stress maximum is reached along the PTP, while for V and Nb the ITS is limited by the bifurcation to the SOP.

Figure 6 shows the variation in the elastic constants of all three metals under uniaxial strain along the [100] direction, referred to a face-centered tetragonal lattice. The important results are the following: (i) within a fct reference frame the condition $c_{22}=c_{23}$ is fulfilled at strains of 0.06, 0.05, and 0.18 for V, Nb, and Ta, respectively. Within a bct reference frame, the condition for a bifurcation is $c_{44}=0$. (ii) At these strains the symmetry will change from tetragonal to orthorhombic under purely uniaxial loading.

The behavior of V and Nb at the bifurcation point differs substantially from that of Ta. For V and Nb the energy-strain curves of the PTP and SOP are tangent at the bifurcation point, the difference between the lattice constants b_2 and b_3 changes continuously, the stress continues to increase after the bifurcation. Hence for V and Nb the branching from the PTP to the SOP is a continuous second order structural transformation from the bct to a face-centered orthorhombic structure induced by purely uniaxial loading which occurs before the ideal tensile strength is reached. For Ta the condition $c_{22}=c_{23}$ (within the fct reference frame) or $c_{44}=0$ (within a bct description of the deformed structure) leads to a shear instability at the stress maximum under uniaxial tension. This means that even under strict uniaxial load, Ta fails not by cleavage but by shear.

The unstable saddle-point configuration reached along the SOP is a "special" bct structure which is energetically degenerate with the metastable fct structure reached at large strains on the PTP. In fact, both structures are related through a rigid rotation about the b_3 axis, the axial ratio of the fct structure is just $1/\sqrt{2}$ times the axial ratio of the bct structure ($a_1/a_2 = 1.81$). At a strain of about 0.41 the energy along the SOP falls to an energy minimum. The configuration corresponding to this minimum is a bcc structure rotated about the b_2 axis relative to the original bcc structure. The restoring strain of $\epsilon=0.41$ is very close to the value of $\epsilon=\sqrt{2}-1=0.414$ calculated for a strictly volume-conserving deformation. The bct saddle-point configuration reached on the SOP under uniaxial $\langle 100\rangle$ loading is identical to that reached under shear along a $\langle 111\rangle$ axis, as will be discussed in more detail below. Hence also along the SOP the bcc metals are predicted to fail not by cleavage, but by shearing.

Hence we find that along the PTP the sequence of the stress-free structures is bcc, fcc, bct [corresponding to scenario (3) discussed by Milstein *et al.*[8,9,11]] for V, Nb, and Ta, as for the other bcc transition metals (Mo, W, Fe) investigated so far. For Ta the criterion $c_{22}=c_{23}$ for a bifurcation to an orthorhombic path is satisfied only for a large strain co-

TABLE II. Ideal tensile strengths σ_{max}, critical strain ϵ_c, Young's modulus $E_{[100]}$ of V, Nb and Ta under uniaxial [100] loading, as determined by the stress maximum along the tetragonal and orthorhombic deformation paths.

			Orthorhombic			Tetragonal		
		$E_{\langle 100\rangle}$	σ_{max}	ϵ_c	$\sigma_{max}/E_{\langle 100\rangle}$	σ_{max}	ϵ_c	$\sigma_{max}/E_{\langle 100\rangle}$
V	This work	160	11.5	0.10	0.07	17.8	0.17	0.11
Nb	This work	148	12.5	0.11	0.09	17.2	0.17	0.12
	Ref. 21	165	13.1	0.12	0.08	18.8	0.18	0.11
Ta	This work	146	13.6	0.16	0.09	13.4	0.16	0.10
Mo	Ref. 21	370				28.8	0.13	0.08
W	Ref. 19	407				29.5	0.13	0.07

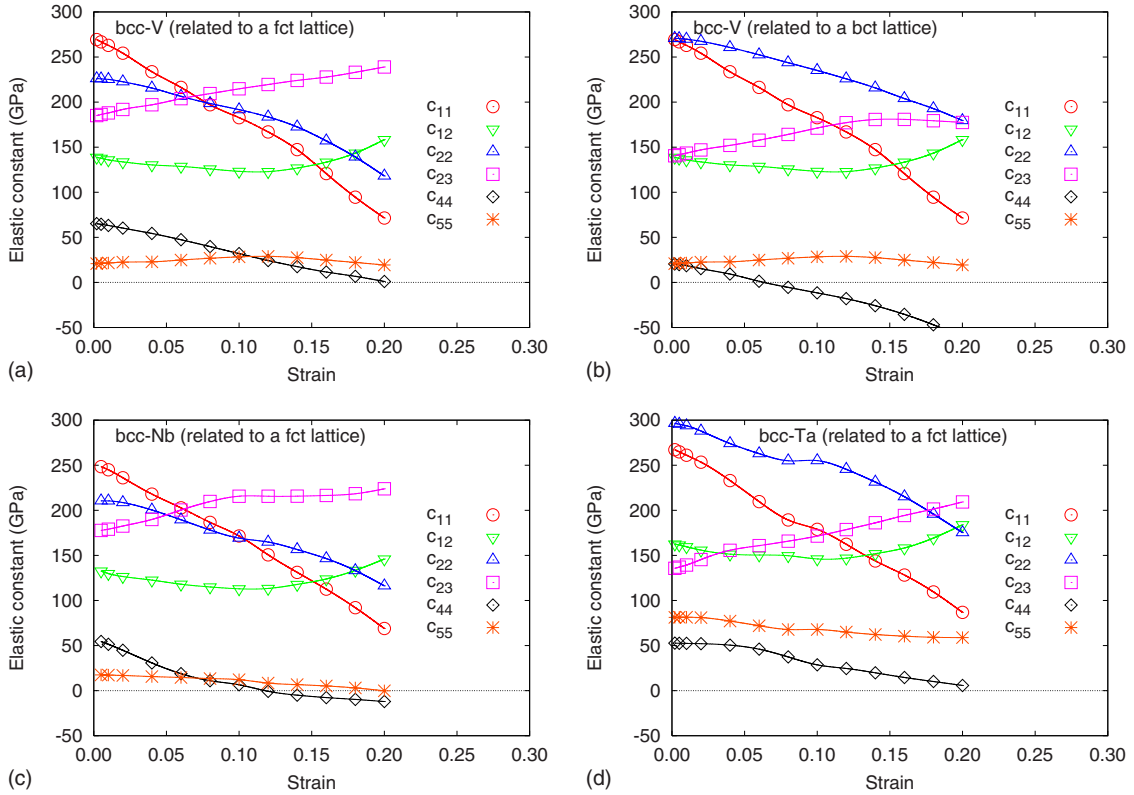

FIG. 6. (Color online) Variation in the elastic constants c_{11}, c_{12}, c_{22}, c_{23}, c_{44}, and c_{55} (related to a face-centered tetragonal lattice) of (a) V, (c) Nb, and (d) Ta along the primary tetragonal deformation path as a function of uniaxial [100] strain. For V we show also the elastic constants related to a bct reference frame (b), in this case the elastic constants reduce to c_{11}, c_{12}, and c_{44} in the bcc limit. Note that the condition for the bifurcation to an orthorhombic lattice is $c_{22}=c_{23}$ in the fct reference frame (contraction/expansion along the fct axes—cf. Fig. 2), but $c_{44}=0$ in the bct reference frame (contraction/expansion along the face-diagonals of the bct basis plane).

incident with the critical strain for tensile failure along the PTP. Hence the situation is similar to that described before for Mo (Ref. 21) and Fe.[32] If the saddle-point structure on the SOP is described within the bct reference frame used for tetragonal deformation under [100] tension, the orthorhombic instability corresponds to a shear instability with $c_{44}=0$. For V and Nb the bifurcation to the SOP occurs already at much smaller strains, the failure mode is determined by the fct saddle-point structure along the SOP. The ITS is reduced from 17.8 GPa to 11.5 GPa for V, and from 17.2 to 12.5 GPa for Nb. The value for Nb is in good agreement with the earlier calculations of Luo it *et al.*[21] For Ta the stress maximum is 13.4 GPa along the tetragonal and 13.6 GPa along the orthorhombic deformation path, i.e the values agree within the computational accuracy. For all three metals the stress-strain curves along the PTP are too asymmetric to be fitted by a sinusoidal curve, leading to a dimensionless ITS of $\sigma^{\star}\sim 0.10-0.12$ which is larger than that calculated for the other bcc transition metals. The stress-strain curve for the SOP is more symmetric, the dimensionless ITS assumes values of 0.07 to 0.09 comparable with those derived for Mo, W, and Fe.

V. RESPONSE TO SHEAR DEFORMATIONS ALONG THE ⟨111⟩ DIRECTION

Figure 7 shows the computational cells used for simulating shear deformations along a ⟨111⟩ direction on the {211} and {110} planes. The undeformed cells are orthorhombic, with lattice parameters a_{SC}, b_{SC}, and c_{SC} as defined in the figure. The shear deformation was applied uniformly to the supercell (affine shear loading). This means that in principle, the calculations could also have been performed with a primitive cell instead. The supercells have been used for computational convenience. With current optimizer relaxation of all transverse stress components to zero values is easier in the supercell geometry.

Because of the threefold rotational symmetry around the ⟨111⟩ axis the relaxed shear modulus $G_{\langle 111\rangle}$ is the same for all common bcc slip systems, {110}⟨111⟩, {211}⟨111⟩, and {321}⟨111⟩ (here we discuss only the former two). Earlier work of Morris *et al.*[19–21,61] on the response of W and Mo to shear loading has demonstrated that the relaxed energy/strain, stress/strain curves, and the ideal shear strengths are very similar for all three slip systems. The changes in symmetry during shear deformation have been discussed in detail by Roundy *et al.*[19] and Krenn *et al.*,[20] using slightly different geometrical arguments. The {110}⟨111⟩ shear system is symmetric, while the {211}⟨111⟩ and {321}⟨111⟩ are not, i.e., slip in the "easy" direction has a lower shear strength than in the "hard" direction. Here we shall restrict our attention to slip in the easy (weak) direction. Upon shearing the bcc lattice parallel to the $(2\bar{1}1)$ plane a mirrored bcc lattice is created at a strain of $\gamma=\sqrt{2}/2\sim 0.71$ (the "twining" strain) if relaxation is excluded. If only a single maximum in the total energy exists for strains from 0 to 0.71, symmetry dictates that it must be

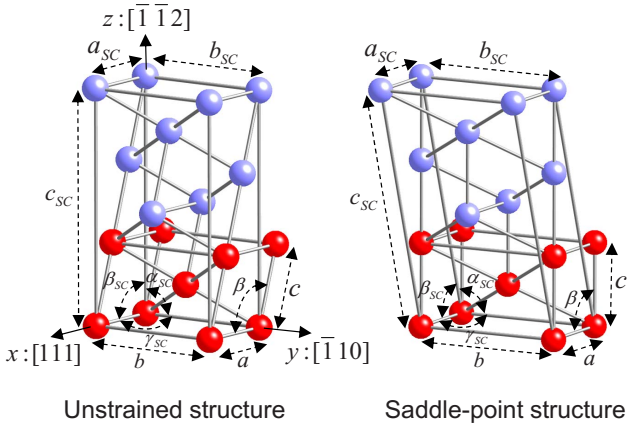

FIG. 7. (Color online) Supercells used to simulate shear deformations along the ⟨111⟩ direction. Part (a) shows the cell used for {211}⟨111⟩ shear, the left part represents the undeformed cell with bcc symmetry, the right part the bct structure at the saddle-point configuration. The primitive cells inscribed in the supercells are shown in red (black). Part (b) shows the starting (bcc) and saddle-point (bct) structures for {110}⟨111⟩ shear. At intermediate strains the symmetry is reduced to monoclinic and triclinic under {211}⟨111⟩ and {110}⟨111⟩ shears, respectively. The monoclinic cells inscribed in the supercells which become the bct cells at the saddle-point structure are indicated by the blue (gray) circles.

located at $\gamma \sim 0.35$, and the inflection point must fall around 0.17. Along this deformation path the symmetry changes from cubic to monoclinic and further to orthorhombic at the saddle point (see Fig. 7). For W it has been found that relaxation has only a very small influence on the stress under (211)[111] strain along the easy direction. This has been attributed to the elastic isotropy of W. Unrelaxed (110)[111] shear reduces the symmetry from cubic to triclinic, the first energy maximum is found when the deformation path passes through a configuration with monoclinic symmetry. For both Mo and W a significantly stronger relaxation has been reported for (110)[111]—relaxation is necessary to recover the bcc structure at a strain of $\gamma \sim 0.6$. For Mo, Luo *et al.*[21] have reported that due to relaxation, the saddle-point structure under (110)[111] shear is very similar to the bct saddle point found for the (211)[111] slip systems. Still, for both Mo and W the stress-strain curves are almost identical for all three slip systems, they have a symmetric sinusoidal shape leading to a reduced shear strength of $\tau_{max}/G_{\langle 111\rangle} \sim 0.11$. Luo *et al.* have also calculated the shear strength of bcc Nb. In this case the stress-strain curves for the (110)[111] and (211)[111] shear systems are more distinctly different than for Mo and more asymmetric, leading to a higher value of the reduced shear strength of ~0.15–0.18, although the actual shear strength is much lower.

The results for the three V-group metals compiled in Figs. 8–10 show that the response of V and Nb on one side and Ta on the other side are significantly different, although the values of the ideal shear strengths are not. For all three metals the ideal shear strength calculated for both slip systems reaches only half the value found for Mo and W in the neighboring column of the Periodic Table. For V and Nb the stress-strain curves are strongly asymmetric—as we shall show below, this is related to a low value of the shear modulus $G_{\langle 111\rangle}$, a strong anisotropy of the elastic shear constants (which is, admittedly, strongly overestimated by the *ab initio* calculations) and strong relaxations under shear loading. For Ta the stress-strain curves are only weakly asymmetric, the reduced shear strength comes close to that calculated for Mo and W.

For V, slightly different saddle-point configurations located at strains of 0.28 and 0.32 are found under {110}⟨111⟩ and {211}⟨111⟩ shear deformations. These differences are related to different degrees of relaxation changing in both cases significantly as a function of strain. Up to a strain of about 0.08 both shears lead to an increase of the lattice constant b_{SC}, a decrease of c_{SC}, while a_{SC} remains almost constant [see Figs. 8(c) and 8(d)]. In this regime only the shearing angle β_{SC} increases linearly with strain, while the other angles remain almost unchanged even under {110}⟨111⟩ shear where the symmetry is reduced to triclinic. Up to this point the deformation occurs at almost constant volume. At a strain of $\epsilon = 0.08$ the lattice constant c_{SC} reaches a minimum. At larger strains the lattice expands strongly along the b_{SC} and c_{SC} directions and contracts by a comparable amount along a_{SC}—together this results in a volume expansion reaching about 1% at the saddle-point configurations and decreasing again at even larger strains. The volume expansion is coupled to a strong increase in energy. Qualitatively, the relaxation pattern is the same for both shear systems, but the variation in the lattice constants is much larger under {211}⟨111⟩ shear while the symmetry remains at least monoclinic at all strains. At the saddle points we find that both lattice constants and angles agree with a bct structure, as shown in Fig. 7. In the saddle-point configurations the monoclinic and triclinic lattices of the {211}⟨111⟩ and {110}⟨111⟩ shear systems adopt tetragonal symmetry, the lattice constants correspond exactly to those determined along the PTP under uniaxial tension (which is just rotated with respect to the bct saddle-point structure reached along the SOP).

The most striking feature, however, is the strongly asymmetric character of the stress-strain curve. Due to the low value of the shear modulus, the stress increases very slowly, the stress-strain curve shows upward curvature. The $G_{\langle 111\rangle}$ shear modulus derived from the initial slope of the stress-strain curve of V is $G_{\langle 111\rangle} = 31.3 \pm 4$ GPa, in reasonable agreement with the value derived from the elastic constants. As discussed above, energy and stress begin to increase at a

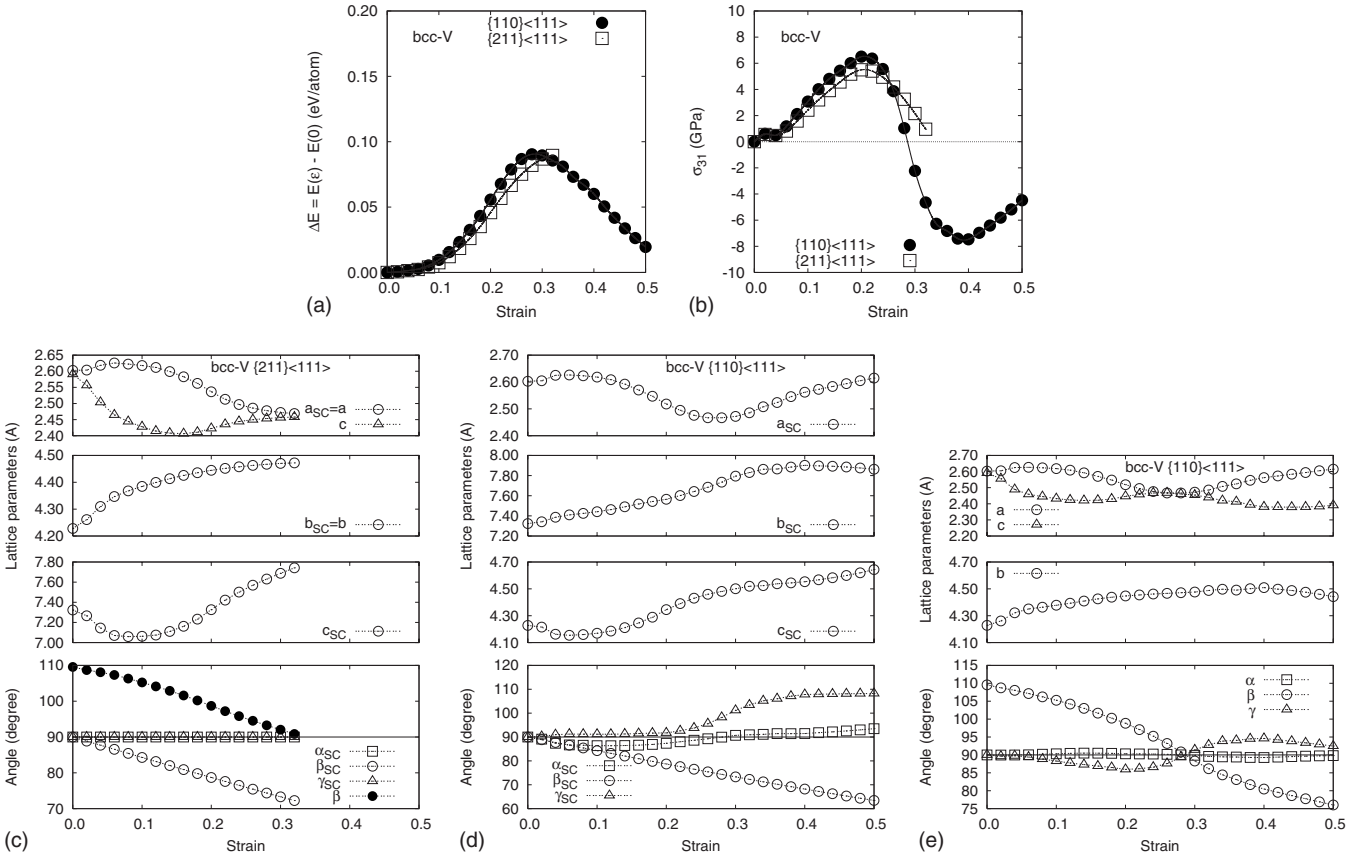

FIG. 8. Variation in (a) the total energy, (b) the stress, (c)–(d) the lattice constants and angles of the computational super-cell, and (e) of the distorted body-centered cell for bcc V as a function of the applied strain under $\{110\}\langle 111\rangle$ and $\{211\}\langle 111\rangle$ shear deformations.

strain large enough such that a pure shear deformation is insufficient to relax all lateral stresses and an expansion of the volume takes place. For both shear systems, the stress maximum is reached at a failure strain of about 0.2—this value is much larger than half of the strain at which the saddle point is located. The ideal tensile strength is 6.5 GPa for shearing along the {110} and 5.5 GPa along the {211} planes, the reduced shear strengths are 0.20 and 0.17, respectively (see Table III). This means that the reduced shear strength is much higher than for Mo and W, although the actual shear strength reaches not even half this value.

Nb shows a behavior under shear which is very similar to that discussed above for V. From the initial slope of the stress-strain curve we calculate a shear modulus of $G_{\langle 111\rangle} \sim 22 \pm 4$ GPa, in good agreement with the elastic constants. A remarkable difference is that the initial contraction of the lattice constant c_{SC} at smaller strains has almost disappeared, and that a_{SC} begins to shrink already at smaller strains. But again we observe a distinct change in the relaxation mode at a strain of $\gamma \sim 0.08$, slightly below the inflection point on the stress-strain curve. At larger strains, relaxation leads to a substantial volume expansion reaching 2% at the saddle-point configuration. The saddle-point structures assumed at $\gamma \sim 0.33$ (for $\{211\}\langle 111\rangle$ shear) and $\gamma \sim 0.29$ (for $\{110\}\langle 111\rangle$ shear) are bct and agree with those assumed on the SOP under uniaxial [100] tension (cf. Figs. 9 and 4). The maximum shear stress is 6.0 GPa (at a failure strain of $\gamma_c = 0.2$) for shearing parallel to the {211} plane, and 7.8 GPa (at $\gamma_c = 0.2$) for shearing along {110}. These values are in good agreement with those of Luo *et al.*,[21] although we find a slightly larger difference between both shear systems. The reduced value of the ideal shear strength is even larger than for V.

For Ta the initial slope of the stress-strain curve yields $G_{\langle 111\rangle} \sim 58 \pm 1$ GPa in excellent agreement with the elastic constants. Only very modest relaxations are observed up to strains of about 0.1. Beyond this point, the lattice constant c_{SC} increases strongly with increasing strain, while b_{SC} and a_{SC} undergo only a more modest expansion and contraction, respectively. These relaxations are also associated with an increasing volume expansion reaching 2% at the saddle point. The saddle-point configurations are reached at $\gamma = 0.29$ (for $\{110\}\langle 111\rangle$ shear) and $\gamma = 0.32$ (for $\{211\}\langle 111\rangle$ shear). The bct lattice constants of the saddle-point structures are $a = c = 2.795$ Å and $b = 4.769$ Å (for $\{211\}\langle 111\rangle$ shear, those for (110)[111] shear agree within 0.01 Å), to be compared with $a = 4.781$ Å, $b = c = 2.792$ Å calculated along the PTP under uniaxial tension. The values of the ideal shear strength are 7.1 (6.5) GPa, at critical strains of $\gamma_c = 0.22(0.20)$ for shearing parallel to the {110} ({211} planes), respectively (see Table III). Although they are much lower than those for Mo and W, all three metals show the same reduced shear strength. Hence for Ta the low value of the ideal shear strength is exactly as expected from the soft elastic shear modulus, while for V and Nb the extremely low shear modulus is not reflected by a similarly low value of the ideal shear strength.

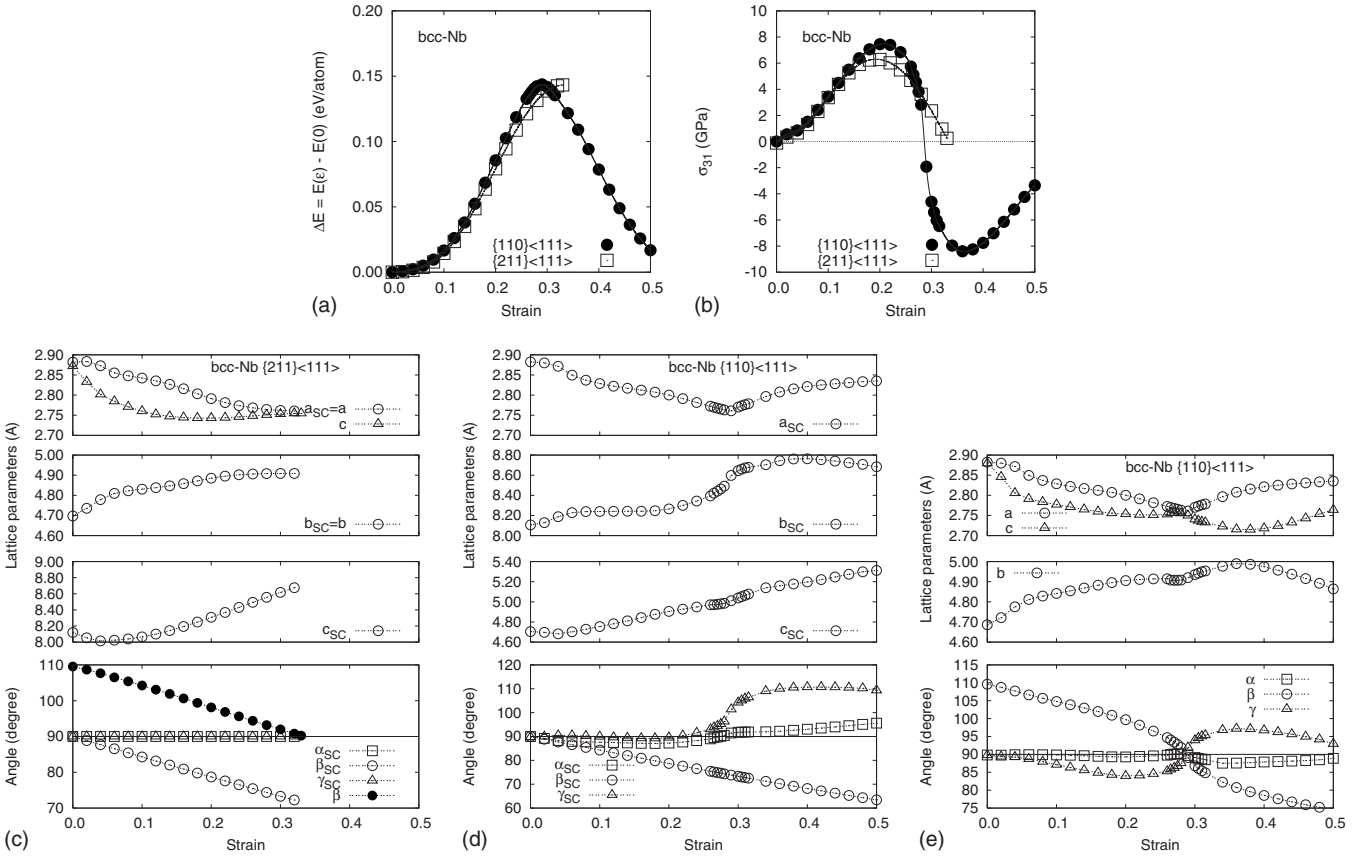

FIG. 9. Variation in (a) the total energy, (b) the stress, (c)–(d) the lattice constants and angles of the computational super-cell and (e) of the distorted body-centered cell for Nb as a function of the applied strain under $\{110\}\langle 111\rangle$ and $\{211\}\langle 111\rangle$ shear deformations.

VI. DISCUSSION AND CONCLUSIONS

We have demonstrated using *ab initio* DFT calculations that the response of body-centered cubic V and Nb to tensile and shear loading differs substantially from that of other bcc transition metals such as Mo, W, and Fe, but also from that of the heaviest metal of the V group, Ta. For these metals the stress-strain curves under tension or shear display a symmetric sinusoidal shape, with a period determined by the nearest extremum on the deformation path. Under uniaxial $\langle 100\rangle$ tension this is a maximum corresponding to a fcc structure adopted under volume conservation at the Bain strain of $\epsilon = \sqrt[3]{2}-1 \sim 0.26$. For all types of shear along the $\langle 111\rangle$ this is a bct structure formed under volume conservation at a shear strain of $\gamma = \sqrt{2}/4 \sim 0.35$, i.e., at half the "twinning" strain recovering the bcc structure. As the initial slope of the stress-strain curve is determined by the relaxed tensile and shear modulus, respectively, the ideal tensile and shear strengths obey the relations

$$\sigma_{max} = \frac{0.26}{\pi} E_{\langle 100\rangle} = 0.08 E_{\langle 100\rangle}, \tag{3}$$

$$\tau_{max} = \frac{0.35}{\pi} G_{\langle 111\rangle} = 0.11 G_{\langle 111\rangle}. \tag{4}$$

For Mo and W the calculated moduli and ideal strength obey these relations with good accuracy. For V and Nb we find that under uniaxial $\langle 100\rangle$ loading a bifurcation from the primary tetragonal to a secondary orthorhombic deformation path occurs before reaching the stress maximum, strongly limiting the ideal tensile strength. Due to a shear instability, an orthorhombic deformation can occur under purely uniaxial load. It is interesting to correlate this shear instability induced by uniaxial strain to the softening of c_{44} under homogeneous compression. It has been shown that for V c_{44} vanishes at a pressure of about 60 GPa, leading to bcc $\rightarrow$rhombohedral structural transition[21,41,42,44] and that this phase transition is associated with the nesting properties of the Fermi surface and an electronic topological transition. While the homogeneous compression of the bcc lattice merely changes the nesting vector, a uniaxial strain changes the symmetry and therefore the topology of the Fermi surface.

The saddle-point structure along the SOP is a special bct structure which can be made to coincide with the fct local energy minimum along the PTP by a rigid rotation and which is also identical to the saddle-point structure under shear deformation. For Ta the bifurcation to the SOP coincides with the stress-maximum along the PTP (as has also been found for Mo). Because the ideal tensile strength is reached at a shear-unstable configuration, Ta fails under uniaxial loading not by cleavage, but by shear. The stress/tensile-strain curves of all three metals are strongly asymmetric along the PTP, but less so along the SOP. This means that the reduced tensile shear strength $\sigma^\star = \sigma_{max}/E_{\langle 100\rangle}$ is about 0.07 to 0.09, only

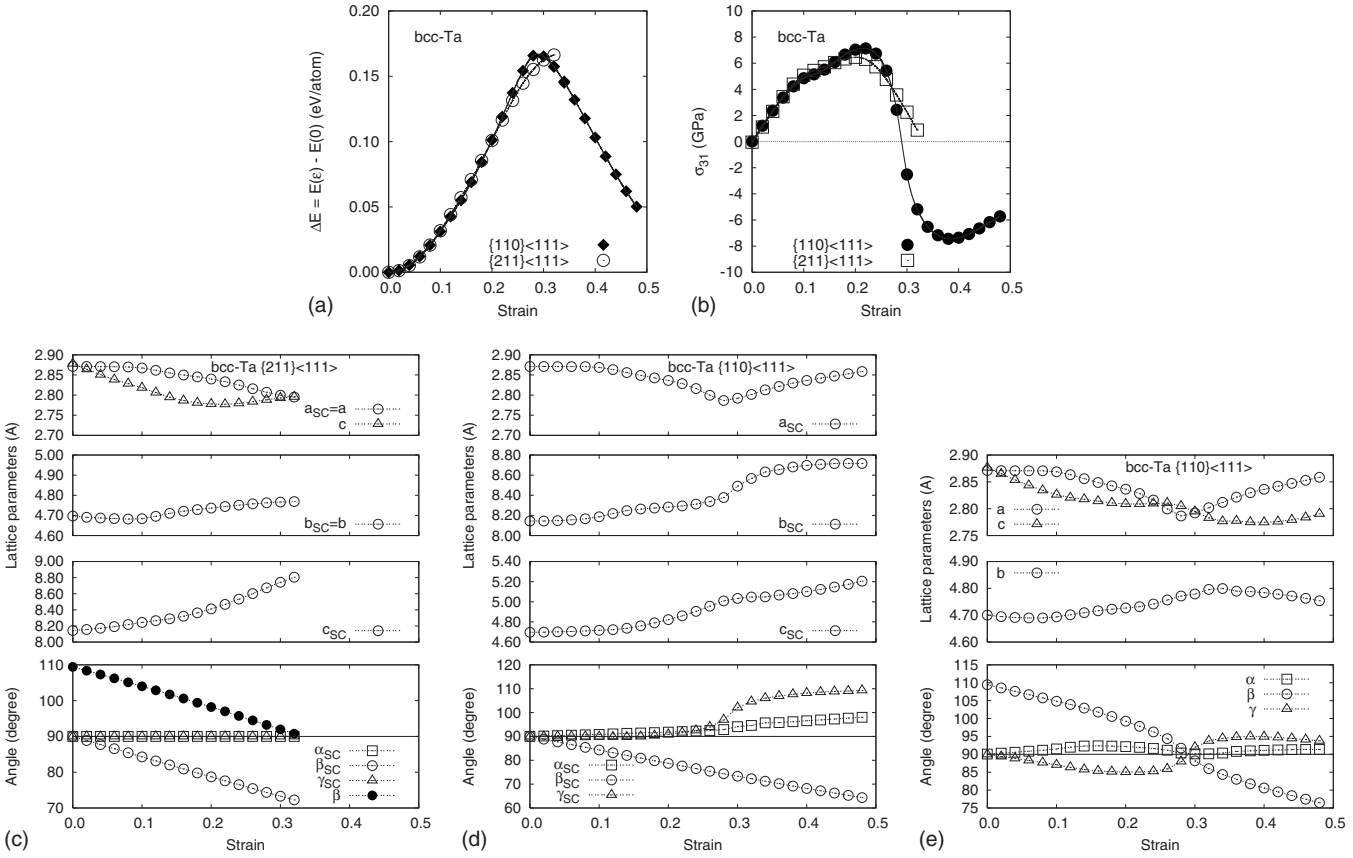

FIG. 10. Variation in (a) the total energy, (b) the stress, (c)–(d) the lattice constants and angles of the computational super-cell, and (e) of the distorted body-centered cell for Ta as a function of the applied strain under $\{110\}\langle 111\rangle$ and $\{211\}\langle 111\rangle$ shear deformations.

slightly larger than for Mo and W, although the ITS is determined by a different saddle-point configuration. Ta is a special case where the bifurcation point coincides with the inflection point on the PTP energy-strain curve. Hence the tetragonal stress maximum is reached at a shear-unstable configuration.

Shearing bcc V or Nb in the $\langle 111\rangle$ direction parallel to a $\{110\}$ or $\{211\}$ planes leads to strongly asymmetric stress-strain curves. A volume conserving unrelaxed $\{211\}\langle 111\rangle$ shear recovers the bcc structure at a strain of $\gamma=\sqrt{2}/2$, hence by symmetry the saddle-point configuration should fall at $\gamma \sim 0.35$ and the inflection point or stress maximum at $\gamma_c \sim 0.175$. However, due to a very low relaxed shear modulus $G_{[111]}$, the initial slope of the stress-strain curve is very low. The stress begins to increase strongly at $\gamma \sim 0.08$ were the relaxation pattern changes qualitatively, accompanied by an incipient volume expansion. The saddle-point structure for both glide systems has bct symmetry, it is reached at strains between 0.28 and 0.32 depending on the glide plane. For $\{110\}\langle 111\rangle$ shear a strong relaxation is required to reach this configuration. This bct saddle-point structure is the same as that reached on the SOP under uniaxial $\langle 100\rangle$ tension. For V the failure strain is $\gamma_c=0.20$, the ideal shear strength is 6.5 and 5.5 GPa for the $\{110\}$ and $\{211\}$ glide planes, respec-

TABLE III. Ideal shear strengths τ_{max}, critical strain γ_c, shear modulus $G_{[111]}$ of V, Nb, and Ta under uniaxial [100] loading, as determined by the stress maximum along the tetragonal and orthorhombic deformation paths.

			$\{110\}\langle 111\rangle$			$\{211\}\langle 111\rangle$		
		$G_{\langle 111\rangle}$	τ_{max}	γ_c	$\tau_{max}/G_{\langle 111\rangle}$	τ_{max}	γ_c	$\tau_{max}/G_{\langle 111\rangle}$
V	This work	33	6.54	0.21	0.20	5.5	0.21	0.17
Nb	This work	31	7.8	0.20	0.25	6.0	0.20	0.19
	Ref. 21		7.6	0.22		6.4	0.20	
Ta	This work	53	7.1	0.22	0.13	6.5	0.201	0.12
Mo	Ref. 21	134	16.1	0.17	0.12	15.8	0.17	0.12
W	Ref. 19	163	18.2	0.17	0.11	18.1	0.17	0.11

tively. The reduced shear strengths are $\tau^*=0.20$ and 0.17—i.e., nearly twice as high as expected for a symmetric stress-strain curve and as calculated for Mo and W. Nb follows the same pattern, with an even slightly larger reduced shear strength.

In summary: (i) For both V and Nb the ideal tensile strength under $\langle 111\rangle$ loading is limited by a bifurcation to an orthorhombic deformation path, but it is still about twice as large as the ideal shear strength for shearing in the $\langle 111\rangle$. (ii) The stress-strain curves for V and Nb under shear deformation are strongly asymmetric, the ideal shear strength is much higher than expected on the basis of a very low shear modulus. This reflects an increasing stiffness of the lattice under increasing shear strain, as shown by the relaxation behavior. (iii) The saddle-point configurations reached under tensile and shear loading have the same special bct structure. For this reason and because the ideal shear strength is much lower than the tensile strength, both metals will fail by shear and not by cleavage. (iv) The response of Ta to tensile and shear loading is more similar to that of Mo or W. However, because the stress maximum under tension is reached at a shear-unstable configuration, Ta will also fail by shear and not by cleavage.

For Ta the ideal shear strength found in our calculations [$\sigma_{max}=7.1(6.5)$ GPa for $\{110\}\langle 111\rangle$ and $\{211\}\langle 111\rangle$ shear] is in excellent agreement with experimental estimates based on nanoindentation measurements[4] yielding an ideal shear strength of about 7.5 GPa. From the nanoindentation experiments and experimental observations of plastic flow response to large strain impact testing[62] it was also suggested the $\{110\}\langle 111\rangle$ slip system is preferred over the $\{211\}\langle 111\rangle$ slip system, but we find only very small differences in the limiting shear strengths and in the critical strains. However, it is certainly encouraging to see that experimental and theoretical determinations of the ideal strength of metals begin to converge.

ACKNOWLEDGMENTS

Work at the University of Vienna has been supported by the VASP project and within the University Research Focus "Material Science" and "Computational Science." We thank T. Bučko for provision of GADGET structural optimization package.

*nagasako@mosk.tytlabs.co.jp
†michal.jahnatek@univie.ac.at
‡rasahi@mosk.tytlabs.co.jp
§juergen.hafner@univie.ac.at

[1] A. Kelly and N. H. MacMillan, *Strong Solids*, 3rd ed. (Clarendon Press, Oxford, 1986).
[2] N. Gane and F. P. Bowden, J. Appl. Phys. **39**, 1432 (1968).
[3] S. G. Corcoran, R. J. Colton, E. T. Lilleodden, and W. W. Gerberich, Phys. Rev. B **55**, R16057 (1997).
[4] M. M. Biener, J. Biener, A. M. Hodge, and A. V. Hamza, Phys. Rev. B **76**, 165422 (2007).
[5] C. A. Schuh, J. K. Mason, and A. C. Lund, Nature Mater. **4**, 617 (2005).
[6] C. A. Schuh, Mater. Today **9**, 32 (2006).
[7] J. Frenkel, Z. Phys. **37**, 572 (1926).
[8] R. Hill and F. Milstein, Phys. Rev. B **15**, 3087 (1977).
[9] F. Milstein and K. Huang, Phys. Rev. B **18**, 2529 (1978).
[10] F. Milstein and B. Farber, Phys. Rev. Lett. **44**, 277 (1980).
[11] F. Milstein, J. Marschall, and H. E. Fang, Phys. Rev. Lett. **74**, 2977 (1995).
[12] F. Milstein and S. Chantasiriwan, Phys. Rev. B **58**, 6006 (1998).
[13] A. T. Paxton, P. Gumbsch, and M. Methfessel, Philos. Mag. Lett. **63**, 267 (1991).
[14] W. Xu and J. A. Moriarty, Phys. Rev. B **54**, 6941 (1996).
[15] P. Alippi, P. M. Marcus, and M. Scheffler, Phys. Rev. Lett. **78**, 3892 (1997).
[16] M. Šob, L. G. Wang, and V. Vitek, Mater. Sci. Eng., A **234-236**, 1075 (1997).
[17] M. Šob, L. G. Wang, and V. Vitek, Philos. Mag. B **78**, 653 (1998).
[18] D. Roundy, C. R. Krenn, M. L. Cohen, and J. W. Morris, Jr., Phys. Rev. Lett. **82**, 2713 (1999).
[19] D. Roundy, C. R. Krenn, M. L. Cohen, and J. W. Morris, Jr., Philos. Mag. A **81**, 1725 (2001).
[20] C. R. Krenn, D. Roundy, J. W. Morris, Jr., and M. L. Cohen, Mater. Sci. Eng., A **319-321**, 111 (2001).
[21] W. Luo, D. Roundy, M. L. Cohen, and J. W. Morris, Jr., Phys. Rev. B **66**, 094110 (2002).
[22] M. Jahnátek, M. Krajčí, and J. Hafner, Philos. Mag. **87**, 1769 (2007).
[23] M. Jahnátek, M. Krajčí, and J. Hafner, Phys. Rev. B **76**, 014110 (2007).
[24] M. Jahnátek, J. Hafner, and M. Krajčí, Phys. Rev. B **79**, 224103 (2009).
[25] J. Pokluda, M. Černy, P. Šandera, and M. Šob, J. Comput.-Aided Mater. Des. **11**, 1 (2004).
[26] D. M. Clatterbuck, C. R. Krenn, M. L. Cohen, and J. W. Morris, Jr., Phys. Rev. Lett. **91**, 135501 (2003).
[27] H. Kitagawa and S. Ogata, Key Eng. Mater. **161-163**, 443 (1999).
[28] S. Ogata and S. Yip, Science **298**, 807 (2002).
[29] S. Ogata, J. Li, and S. Yip, Phys. Rev. B **71**, 224102 (2005).
[30] M. Černy, M. Šob, J. Pokluda, and P. J. Šandera, J. Phys.: Condens. Matter **16**, 1045 (2004).
[31] M. Šob, L. G. Wang, and V. Vitek, Kovove Mater. **36**, 145 (1998).
[32] D. M. Clatterbuck, D. C. Chrzan, and J. W. Morris, Jr., Acta Mater. **51**, 2271 (2003).
[33] M. Friák, M. Šob, and V. Vitek, Philos. Mag. A **83**, 3529 (2003).
[34] M. Jahnátek, M. Krajčí, and J. Hafner, (unpublished).
[35] W. Luo, M. L. Cohen, and J. W. Morris, Jr., Philos. Mag. Lett. **89**, 23 (2009).
[36] J. Trivisonno, S. Vatanayon, M. Wilt, J. Washick, and R. Reifenberger, J. Low Temp. Phys. **12**, 153 (1973).
[37] K. W. Katahara, M. H. Manghnani, and E. Fisher, J. Phys. F: Met. Phys. **9**, 773 (1979).

[38] H. Kojima, M. Shino, and T. Suzuki, Acta Metall. **35**, 891 (1987).
[39] F. H. Featherston and J. R. Neighbours, Phys. Rev. **130**, 1324 (1963).
[40] K. W. Katahara, M. H. Manghnani, and E. Fisher, J. Appl. Phys. **47**, 434 (1976).
[41] A. Landa, J. Klepeis, P. Söderlind, I. Naumov, O. Velikokhatnyi, L. Vitos, and A. Ruban, J. Phys.: Condens. Matter **18**, 5079 (2006).
[42] L. Koči, Y. Ma, A. R. Oganov, P. Souvatzis, and R. Ahuja, Phys. Rev. B **77**, 214101 (2008).
[43] P. Söderlind, O. Eriksson, J. M. Wills, and A. M. Boring, Phys. Rev. B **48**, 5844 (1993).
[44] Y. Ding, R. Ahuja, J. Shu, P. Chow, W. Luo, and H. K. Mao, Phys. Rev. Lett. **98**, 085502 (2007).
[45] T. Kenichi and A. K. Singh, Phys. Rev. B **73**, 224119 (2006).
[46] Y. Nakagawa and A. D. B. Woods, Phys. Rev. Lett. **11**, 271 (1963).
[47] R. Colella and B. W. Batterman, Phys. Rev. B **1**, 3913 (1970).
[48] W. Luo, R. Ahuja, Y. Ding, and H. Mao, Proc. Natl. Acad. Sci. U.S.A. **104**, 16428 (2007).
[49] C. M. Varma and W. Weber, Phys. Rev. B **19**, 6142 (1979).
[50] G. Kresse and J. Furthmüller, Comput. Mater. Sci. **6**, 15 (1996).
[51] G. Kresse and J. Furthmüller, Phys. Rev. B **54**, 11169 (1996).
[52] J. P. Perdew, J. A. Chevary, S. H. Vosko, K. A. Jackson, M. R. Pederson, D. J. Singh, and C. Fiolhais, Phys. Rev. B **46**, 6671 (1992).
[53] P. E. Blöchl, Phys. Rev. B **50**, 17953 (1994).
[54] G. Kresse and D. Joubert, Phys. Rev. B **59**, 1758 (1999).
[55] T. Bučko, J. Hafner, and J. G. Ángyán, J. Chem. Phys. **122**, 124508 (2005).
[56] R. P. Feynman, Phys. Rev. **56**, 340 (1939).
[57] O. H. Nielsen and R. M. Martin, Phys. Rev. Lett. **50**, 697 (1983).
[58] H. J. Monkhorst and J. D. Pack, Phys. Rev. B **13**, 5188 (1976).
[59] M. Methfessel and A. T. Paxton, Phys. Rev. B **40**, 3616 (1989).
[60] P. E. Blöchl, O. Jepsen, and O. K. Andersen, Phys. Rev. B **49**, 16223 (1994).
[61] J. W. Morris, Jr., C. R. Krenn, D. Roundy, and M. L. Cohen, in *Phase Transformations and Evolution in Materials*, edited by P. E. Turchi and A. Gonis (TMS, Warrendale, PA, 2000), p. 187.
[62] P. J. Maudlin, J. F. Bingert, and G. T. Gray, Int. J. Plast. **19**, 483 (2003).